Basin-scale development of giant collapse structures induced by gypsum diagenesis

Jimmy Moneron[*,1], and Christopher Aiden-Lee Jackson[2,3]

[1]*Department of Earth Sciences, University of Oxford, Oxford OX1 3AN, UK*

[2]*WSP UK Ltd, 8 First Street, Manchester, M15 4RP, UK*

[3]*Landscape and Basins Research Group (LBRG), Department of Earth Science and Engineering, Imperial College London, London SW7 2AZ, UK*

ABSTRACT

Across buried sedimentary basins, the dissolution-prone nature of evaporite sequences drives the formation of collapse structures (e.g., sinkholes), fundamentally transforming landscapes at large scales. Understanding where, why, and how such structures form is crucial, given they pose geological hazards that may threaten human safety and infrastructure stability, or may affect subsurface resource extraction and geological storage. Here, we use 3D seismic reflection and borehole data from the Southern North Sea Basin to document giant (km-wide and several hundred-metres deep) collapse structures within the upper part of the evaporite-dominated, Zechstein Supergroup (Permian). We show that these features, which form both isolated, sub-circular sinkholes and polygonal, valley-like networks, are developed at the basin-scale (>10,000km^2). Critically, these structures invariably overlie gypsum buildups capped by thick halite deposits (100–300m), with seismic-stratigraphic relationships enabling precise dating and facilitating accurate

modelling. We propose that the transformation of gypsum to anhydrite during early burial initiated the extrusion of NaCl-undersaturated water, which provoked hypogenic dissolution of the capping halite, leading to collapse at the depositional surface. The resulting Permian landscape was buried and thus preserved by a potash infilling unit. To the best of our knowledge, the basin-wide development of this type of giant salt dissolution-induced collapse structure has not previously been described in the stratigraphic record.

INTRODUCTION

Geomorphological depressions can form due to the subsurface dissolution of rocks, being widely documented on Earth and other planetary bodies (e.g., De Mille, et al., 1964; Adams et al., 2009). In evaporite-dominated successions, these structures form in response to chemical saturation imbalances within percolating pore fluids, more specially where NaCl-undersaturated fluids encounter highly soluble rocks such as halite. This process can create large (>10m wide and deep), aerally extensive (i.e., up to several km^2), subsurface cavities evolving into collapse structures, such as sinkholes or dolines (e.g., Arkin and Gilat, 2000). These dissolution-induced structures, extensively described in the rock record (e.g., Hardage, et al., 1996), pose significant (geo)hazards to human safety and industrial operations, where evaporite dissolution renders areas unstable and largely uninhabitable (e.g., Arkin and Gilat, 2000).

In addition to dissolution by fluids undersaturated with respect to a specific chemical phase, there are several other diagenetic processes that may occur during early burial of evaporite-dominated sequences. For example, the transformation of gypsum ($CaSO_4 \cdot 2H_2O$) to anhydrite ($CaSO_4$), a reversible de-re-hydration reaction, can result in substantial volume/density changes in the subsurface rock mass, as well as liberating pore water (Stewart, 1963). In layered evaporite

sequences (LES; *sensu* Rowan et al., 2019), which comprises a mixture of evaporite and other rock types, a variety of coupled diagenetic-dissolution-deformation processes should occur. Whereas traditional methods, such as the analysis of mine or surface exposures, are constrained by the scale and/or lack of broad stratigraphic context, imaging by 3D reflection seismic reflection data can help determine the presence, geometry, distribution, and genesis of salt dissolution-induced deformation. Here we use these data to study the Zechstein Supergroup (ZSG) LES, a pan-European, Permian stratigraphic unit that records polycyclic deposition of carbonate, clastic, and evaporite rocks (Taylor, 1998). Because of: 1) nearly continuous imaging by 3D seismic reflection data; 2) extensive borehole data; and 3) a well-established, trans-national stratigraphic framework, it is an outstanding geological laboratory for investigating dissolution-induced collapse structures within LES. We focus on the third Zechstein cycle (Z3), and more specifically on the spatial and possibly genetic relationship between anomalously thick zones (ATZs, Fig. 1aa', Moneron, 2025) of anhydrite and overlying potash-filled depressions.

STRATIGRAPHIC FRAMEWORK

In the North Sea, the ZSG comprises five main seismo-stratigraphic units (Z1-5, e.g., Smith and Crosby, 1979; Geluk, 1999) (Figs. 1, 2; Fig. S1, Supp. Material[1]). The Z3 cycle includes the ~50m-thick, anhydrite-dominated Z3a, the 100–200m-thick, halite-dominated Z3h, and the K-Mg-rich Z3k potash layer, locally up to 90m thick (Smith and Crosby, 1979; Taylor, 1998). Z3a contains anomalously thick (up to ~150 m compared to a background thickness of ~45m) zones (ATZs, van Gent et al., 2011, Moneron, 2025; Fig. 2D-G), interpreted as syn-depositional

gypsum build-ups (Moneron, 2025). These ATZ networks are mapped across the South Permian Basin (Fig. 1) and are capped by halite (Z3h), followed by Z3k, a basin-wide K-Mg-rich unit comprising sylvinite, carnallite, kieserite, and bischofite (Coelewij et al., 1978; Raith et al., 2017). Z3k reflects extreme hydrological isolation and desiccation (e.g., Czapowski and Bukowski, 2010), with its with highly variable proportions of K-Mg salt (e.g., sylvite, carnallite and bischofite) linked to basin physiography, diagenesis, and intra-Z3k deformation (e.g., Raith et al., 2017). The Z3k thickness variability is attributed to halokinesis and salt remobilisation (Smith and Crosby, 1979). Z3k is capped by the *Roter Salzton* or "red salt clay", a ~15 m-thick, isopachous layer (Grant et al., 2019) defining the transition to the Z4 unit (Richter-Bernburg, 1955), conformably overlying the upper Z3k sequence continuous reflections (Fig. 2)

DATA AND METHODS

Seismic And Well Data

We use ~16,000km² of 3D seismic data from the Southern North Sea, primarily the SNS MegaSurvey (PGS, 2015), which merges 86 individual surveys, and the Cavendish survey (WesternGeco) (Fig. 1). Both datasets share comparable polarity and resolution. Data are displayed with SEG "normal" polarity and zero-phase wavelets, i.e., a downward increase and decrease in acoustic impedance are defined by positive (red) and negative (blue) reflections, respectively. Nineteen wells (Figs. 1, S3) were used to generate seismic-to-well ties and to analyse the lithology and stratigraphic architecture of the Z3 (Fig. S2). Wells were chosen based on available petrophysical logs and VSP data, and clear evidence from seismic data that they penetrate Z3k.

*A "**Seismic-To-Well Tie And Mapping**" section is provided in the Supp. Material*

RESULTS

The basal unit of the Z3 sequence, Z3a, is laterally extensive and predominantly composed of anhydrite, with claystone layers. Borehole and seismic data show that Z3a is locally defined by anomalously thick zones of anhydrite (van Gent et al., 2011; Moneron, 2025). These ATZs have a continuous basal reflection (Base Z3) and an elevated, though sometimes discontinuous, upper surface (Top Z3a) (Moneron, 2025 e.g., Fig. S5b-d). Moneron (2025) shows that the ATZs are developed across the studied portion of the South Permian Basin, forming an extensive (> 100km), interconnected network of sinuous ridges and elliptical mounds, with individual segments extending over tens of kilometres (Fig. 3A).

The overlying Z3h is expressed in seismic reflection data by weakly to moderately, locally chaotic reflections (lower part) and more continuous, sub-horizontal, stronger reflections (upper part). It forms a regionally and lithologically consistent layer of massive halite with minor anhydrite inclusions (Fig. 2). In undeformed areas, Z3h maintains a relatively uniform thickness, except in areas where it thins across ATZs in Z3a (Fig. 2D, 2F). Critically, borehole cuttings reveal that anhydrite inclusions in Z3h are predominantly located near its basal contact with Z3a (Fig. 2), with more of these inclusions appearing in the regions between the base Z3k depressions and underlying ATZs (e.g., Fig. 2G).

Z3h halite is overlain by a base Z3k irregular surface, along which 1km wide and 300m deep depressions are developed (Figs. 2D, 2F). The depressions flanks dip 10-20°, and exhibit a distinct, "stepped, staircase-like" morphology (e.g., centre left of Fig. 3B), clearly truncating

underlying Z3h halite (Figs. 3C-D). In map-view, the 1->10km long and 0.5-1.5km wide base-Z3k depressions are elongate, curvilinear, or sub-circular (Figs. 3B-C). Notably, they directly overlie and mimic the geometry of the underlying ATZ networks (Fig. 3A, Moneron, 2025).

The irregular surface defining the base of Z3k is capped by regionally correlatable, sub-horizontal layers of K-Mg salts (mainly sylvite, carnallite, and polyhalite), with variable proportions of intercalated halite (Figs. 2, S2-S4). Z3k contains a relatively thick (10s of m) layer of K-Mg salts that that is identified in cuttings, defined by a distinct shift to high GR values, and is expressed as a high-amplitude reflection in seismic data, allowing regional mapping across most studied wells.

Noteworthily, Z3k thickens by up to 250% into the base-Z3k depressions, where sub-horizontal reflections in the lower half of Z3k are observed to onlap the flanks of these depressions (Fig. 3C-G). Borehole data also show that base-Z3k depressions controlled not only the bulk thickness of Z3k, but also its composition, as the ratio of K-Mg salts to halite in Z3k is significantly higher within the base-Z3k depressions (i.e., above the ATZs of Z3a; Fig. 2G). Importantly, thickness and lithology variations in Z3k appear independent of the structural configuration of the underlying Z3a, remaining isopachous irrespective of whether Z3a is sub-horizontal or folded (Fig. S5E-G). Further analysis of borehole and seismic data reveals that the base-Z3k depressions are aligned above the ATZs (Moneron, 2025), with thicker Z3k sequences (113m vs. 74m in non-ATZ areas; Fig. 2, Fig. S7) overlying relatively thin Z3 halite (Z3h) and the deeper ATZs (Figs. 2C-F).

INTERPRETATION AND DISCUSSION

From Gypsum Buildups To Salt Collapse

While we have established that the depressions are collapse features (evidenced by the truncation of the underlying Z3h halite, Fig. 3C) rather than structural formations caused by halokinesis, a key question arising from our data is: “Why do the base-Z3k depressions consistently align with ATZs in the Z3a anhydrite?”. Based on their spatial relationship, observations from other salt basins, and the composition of the Z3 unit, we propose that the answer may lie in diagenetic transformations during early burial.

Following ATZ accumulation and a shift in brine chemistry from gypsum to halite saturation (Fig. 4A), early burial triggered the transformation of Z3a gypsum to anhydrite (e.g., Peryt et al., 2010), releasing 30-40% of its rock volume as mineral-bound water (Borchert and Baier, 1953; Langbein, 1987). Loading by the overlying halite caprock led to compaction, increased pore pressure (Fig. 4B), and hydrofracturing along fractures and bedding planes. These fractures provided pathways for the upward migration of NaCl-undersaturated brines, which, upon contact with halite, induced thermal-chemical disequilibrium, dissolution, fluid mobility, and destabilising the caprock, leading to its collapse (Fig. 4C). Anhydrite inclusions in the lowermost Z3h are consistent with anhydrite precipitation from upward-flowing fluids (Fig. 2G) (Behlau and Mingerzahn, 2001). These linked processes seem similar to hypogene karst formation in other sedimentary basins (Bayari et al., 2009), where thermodynamic processes drive the upward migration of overpressured, undersaturated fluids. This genetic link explains why the curvilinear and elongated geometries of the base-Z3k depressions (Fig. 3) mimic those of the underlying Z3a anhydrite networks.

Our model requires anhydritisation at ~300 m burial depth (c. 100-150 ms with halite velocity of ~4.5km/s; Grant et al., 2019). Assuming surface temperatures of 25–35°C during Z3h halite deposition (e.g., in the Dead Sea; Sirota et al., 2017) and a geothermal gradient of 30°C/km (Gluyas et al., 2018), Z3a would have reached >40°C, optimal for gypsum dehydration (Stewart et al., 1963; Hardie, 1967). This interpretation also aligns with documented Z3k composition alterations, attributed to gypsum dewatering in the underlying Z3a (Borchert and Muir, 1964).

Impact of diagenesis-induced collapse on the Permian landscape and deposition

As described above, the base-Z3k depressions controlled lithology variations in the Z3k sequence, with the depressions being enriched in K-Mg salt (Fig. 2). Z3h halite deposition terminated with episodic exposure and desiccation of the basin floor, under isolated, shallow-water conditions, leading to the accumulation of the Z3k unit (Fig. 4C) (e.g., Czapowski et al., 2012; Raith et al., 2017). The stepped, staircase-like flanks of the base-Z3k depressions (e.g., centre left of Fig. 3B), resembling marine terraces formed during sea-level fall (cf. retreating coastline of the Dead Sea; Ghazleh and Kempe, 2009), suggest basin desiccation and punctuated Z3k deposition, driven by evaporation-refreshing cycles that fluctuated salinity (Krupp, 2005) and deposited alternating halite and K-Mg salts on the depression flanks (e.g., Borchert and Muir, 1964; Raith et al., 2017). The Z4 *Roter Salzton* (Richter-Bernburg, 1955), capping the Z3k unit (Fig. 2-3), indicates the eventual establishment of marine conditions (Fig. 4D).

Implications

The coupled diagenetic, fluid flow, and dissolution processes we describe offer a framework for interpreting analogous features in salt basins globally. For example, gypsum-rich basins, like the Dead Sea, are also deformed by sinkholes (Arkin and Gilat, 2000), which may also be caused by hypogenic evaporite dissolution, similar to the mechanisms proposed here. Salt basins influenced by early salt tectonics, particularly those containing hydrated sulphate deposits (e.g., Célini et al., 2024), could develop anomalously locally thickened lithologies within an LES, preconditioning them for spatially variable, diagenesis-induced deformation in a similar way to that documented here. As such, understanding the distribution of underlying thickness variations in evaporites, associated with the subsurface temperature and pressure regime, is critical.

CONCLUSIONS

This research highlights the role of gypsum diagenesis in shaping evaporite-bearing basins, exemplified by the Zechstein Basin. Analysis of 3D seismic and borehole data reveals a multi-stage process where gypsum-to-anhydrite transformation releases pore water, triggering halite dissolution and forming collapse structures later infilled with potash. The alignment of depressions with gypsum mounds underscores how thickness heterogeneities influence surface stability, offering a new framework for understanding large-scale salt collapse and its global implications.

ACKNOWLEDGEMENTS

This research was carried out under the Agile Initiative, supported by the Natural Environment Research Council as part of the Changing the Environment Programme – NERC grant reference number NE/W004976/1. We are grateful to Schlumberger for providing the Petrel academic licenses. B. Aldridge, D. Phillips, and J. Cartwright are thanked for their meaningful insights and engaging discussions. Mike Kendall (Head of the Department, University of Oxford) is thanked for his support in publishing this paper. Seismic (SNS MegaSurvey) and well datasets are provided by the North Sea Transition Authority and/or other third parties.

REFERENCES CITED

Adams, J. B., Gillespie, A. R., Jackson, M. P. A., Montgomery, D. R., Dooley, T. P., Combe, J. P., & Schreiber, B. C. (2009). Salt tectonics and collapse of Hebes Chasma, Valles Marineris, Mars. *Geology*, *37*(8), 691-694.

Arkin, Y., & Gilat, A. (2000). Dead Sea sinkholes–an ever-developing hazard. *Environmental Geology*, *39*, 711-722.

Bayari, C. S., Pekkan, E., & Ozyurt, N. N. (2009). Obruks, as giant collapse dolines caused by hypogenic karstification in central Anatolia, Turkey: analysis of likely formation processes. Hydrogeology Journal, 17(2), 327.

Behlau, J., Mingerzahn, G., 2001. Geological and tectonic investigations in the former Morsleben salt mine (Germany) as a basis for the safety assessment of a radioactive waste repository. Eng. Geol. 61, 83–97. https://doi.org/10.1016/S0013-7952 (01)00038-2.

Borchert, H. & Baier, E. Zur Metamorphose ozeaner Gipsablagerungen. Neues Jahrb. Für

Mineral. Abh. B 86, 103–154 (1953).

Borchert, H. & Muir, R., 1964. Salt deposits: the origin, metamorphism and deformation of evaporites. Van, D. Nostrand Company Ltd (Salzgitter).

Célini, N., Pichat, A., & Ringenbach, J. C. (2024). Salt tectonics synchronous with salt deposition in the Santos Basin (Ariri Formation, Brazil). Earth and Planetary Science Letters, 641, 118853.

Coelewij, P., Haug, G. & Van Kuijk, H. 1978. Magnesium-salt exploration in the northeastern Netherlands. Geologie en Mijnbouw 57(4): 487–502

Czapowski, G., & Bukowski, K. (2010). Geology and resources of salt deposits in Poland: the state of the art. *Geological Quarterly*, *54*, 509-518.

Czapowski, G., Tomassi-Morawiec, H., Toboła, T., & Tadych, T. (2012). Geology, geochemistry and petrological characteristics of potash salt units from PZ2 and PZ3 Zechstein (Late Permian) cycles in Poland. *Geol. Geophys. Environ*, *38*(2), 153-188.

De Mille, G., Shouldice, J. R., & Nelson, H. W. (1964). Collapse structures related to evaporites of the Prairie Formation, Saskatchewan. *Geological Society of America Bulletin*, *75*(4), 307-316.

Geluk, M., 1999. Late Permian (Zechstein) rifting in the Netherlands; models and implications for petroleum geology. Petroleum Geoscience, 5, 189–199.

Ghazleh, S. A., and Kempe, S., 2009, Geomorphology of Lake Lisan terraces along the eastern coast of the Dead Sea, Jordan, Geomorphology, 108, 246-263.

Gluyas, J. G., Adams, C. A., Busby, J. P., Craig, J., Hirst, C., Manning, D. A. C., ... & Younger, P. L. (2018). Keeping warm: a review of deep geothermal potential of the UK. *Proceedings of the Institution of Mechanical Engineers, Part A: Journal of Power*

and Energy, *232*(1), 115-126.

Grant, R. J., Underhill, J. R., Hernández-Casado, J., Barker, S. M., & Jamieson, R. J. (2019). Upper Permian Zechstein Supergroup carbonate-evaporite platform palaeomorphology in the UK southern North Sea. Marine and Petroleum Geology, 100, 484-518.

Hardage, B. A., Carr, D. L., Lancaster, D. E., Simmons Jr, J. L., Elphick, R. Y., Pendleton, V. M., & Johns, R. A. (1996). 3-D seismic evidence of the effects of carbonate karst collapse on overlying clastic stratigraphy and reservoir compartmentalization. *Geophysics*, *61*(5), 1336-1350.

Hardie, L.A., 1967. The gypsum–anhydrite equilibrium at one atmosphere pressure. American Mineralogist, 52, 171–200.

Herrmann, A.G., Rühe, S., and Usdowski, E., 1997. Fluid Inc1usions: Neue Erkenntnisse über den Stoffbestand NaCI-gesättigter Meerwasserlösungen im Zechstein 3. - Kali u. Salz, 12 (4): 1 1 5-125.

Krupp, R. E. (2005). Formation and chemical evolution of magnesium chloride brines by evaporite dissolution processes—Implications for evaporite geochemistry. *Geochimica et Cosmochimica Acta*, *69*(17), 4283-4299.

Langbein, R. The Zechstein sulphates: The state of the art. in *The Zechstein Facies in Europe* (ed. Peryt, T. M.) vol. 10 143–188 (Springer-Verlag, Berlin/Heidelberg, 1987).

Moneron, J., 2025. Major heterogeneity in evaporitic depositional systems: The genesis of kilometre-scale gypsum networks in the Zechstein Basin. *Global and Planetary Change*, 104710. https://doi.org/10.1016/j.gloplacha.2025.104710

Peryt, T.M., et al., 2010. Sulphur and oxygen isotope signatures of late Permian Zechstein anhydrites, West Poland: seawater evolution and diagenetic constraints. Geological

Quarterly, 54, 387–400.

Raith, A.F., Strozyk, F., Visser, J., & Urai, J.L., 2017. Evolution of rheologically heterogeneous salt structures: a case study from the NE Netherlands. Solid Earth, 7, 67–82.

Richter-Bernburg, G., 1955. Stratigraphische Glie-derung des deutschen Zechsteins. Z. dt. geol. Ges. 105, 843-54.

Rowan, M.G., Urai, J.L., Fiduk, J.C. & Kukla, P.A., 2019. Deformation of intrasalt competent layers in different modes of salt tectonics. *Solid Earth*, 10(3), pp.987-1013.

Schachl, E., 1991. Das Steinsalzbergwerk Braunschweig-Lüneburg, Schichtlagerung in der Wurzelzone eines Salzstocks. Zentralblatt Für Geol. Paläontol. 1, 1223–1245.

Sirota, I., Enzel, Y., & Lensky, N.G., 2017. Temperature seasonality control on modern halite layers in the Dead Sea: In situ observations. Geological Society Bulletin, 129, 1181–1194.

Smith, D. B. and Crosby, A., 1979. The regional and stratigraphical context of Zechstein 3 and 4 potash deposits in the British sector of the southern North Sea and adjoining land areas. Economic Geology, 74, 397-408.

Stewart, F. H. (1963). *Marine evaporites*. US Government Printing Office.

Taylor, J.C.M., 1998. Upper Permian—Zechstein, in: Petroleum Geology of the North Sea. John Wiley & Sons, Ltd, pp. 174–211.

van Gent, H., Urai, J.L., De Keijzer, M., 2011. The internal geometry of salt structures – A first look using 3D seismic data from the Zechstein of the Netherlands. Journal of Structural Geology, 33, 292–311.

Warren, J.K., 2006. Evaporites: Sediments, Resources, and Hydrocarbons. Springer.

Williams-Stroud, S.C., & Paul, J., 1997. Initiation and growth of gypsum piercement structures

in the Zechstein Basin. Journal of Structural Geology, 19, 897–907

FIGURE CAPTIONS

Fig. 1 Map showing study area, seismic reflection data extent, (black polygons with transparent fill—SNS Megasurvey; red polygon—Cavendish survey) and the distribution of collapse structures**.** The dots represent the wells colour-coded as shown in Fig. 2, and located in Fig. S2. Paleogeography (inset) modified after Geluk (1999) and Taylor (1998). *aa'*: Profile showing the internal stratigraphy of the ZSG. Salt collapse-prone areas are interpreted from underlying ATZ networks (Moneron, 2025). ATZ—Anomalously Thick Zone. UK—United Kingdom. NL—Netherlands. NPB—Northern Permian Basin. SPB—Southern Permian Basin. PB—Polish Basin. MNSH—Mid North Sea High. The bathymetric map is modified from emodnet.eu/. Coordinates are in degrees (UTM WGS84).

Fig. 2 A-B. Well-tied seismic sections imaging the ZSG, showing the general geophysical expression of the unit, as well as the base-Z3k collapse structures and associated ATZs (located in Fig. 1). **C-F.** Seismic sections showing thickness variations in the Z3k unit and its relationship to ATZs in the lower part of the Z3 interval. **G.** Stratigraphic correlation (datum=base Z4) through the areas shown in (C-F). Location of the four wells in Fig. 1. For the graphs in (G), 19 wells were analysed: 13 crossing a flat base Z3k surface and 6 penetrating base Z3k depressions spatially aligned with underlying ATZs (Table of Fig. S7).

Fig. 3. A. Location of enlargements, ATZ networks, and cross-sections for Z3k thickness assessment. **B-C.** Structure maps of the base Z3k, highlighting depressions and associated stratigraphic relationships. The white dashed polygon in B represents a data gap caused by a

dyke. **D.** Typical Z3k depression over an ATZ, with truncation patterns, Z3k onlaps, and a schematic representing metrics for measuring normalised thickness variations (in G). **E.** Thickness map of the Z3k layer. **F.** Upper inset: Dip map of the base Z3k with a 10° cutoff, corresponding to ~35 ms thickness (lower inset). **G.** Normalised Z3k thickness distributions, showing a distinct thickness increase over ATZs (~30 cross sections analysed, Table of Fig. S7).

Fig. 4. Four-stage conceptual model for the genesis of potash-filled depressions in the Zechstein Basin. **A**. Formation of gypsum ATZs during Z3a deposition. **B**. Burial under Z3h halite and compaction of gypsum layers. **C**. Gypsum dehydration to anhydrite releases brines, inducing halite dissolution, subsidence, and collapse. **D**. Depressions infilled with K-Mg salts during Z3k deposition, transitioning to stability with Z4 claystones. **Insets**: Cross-sectional views of evolving topography.

FIGURES

Figure 1

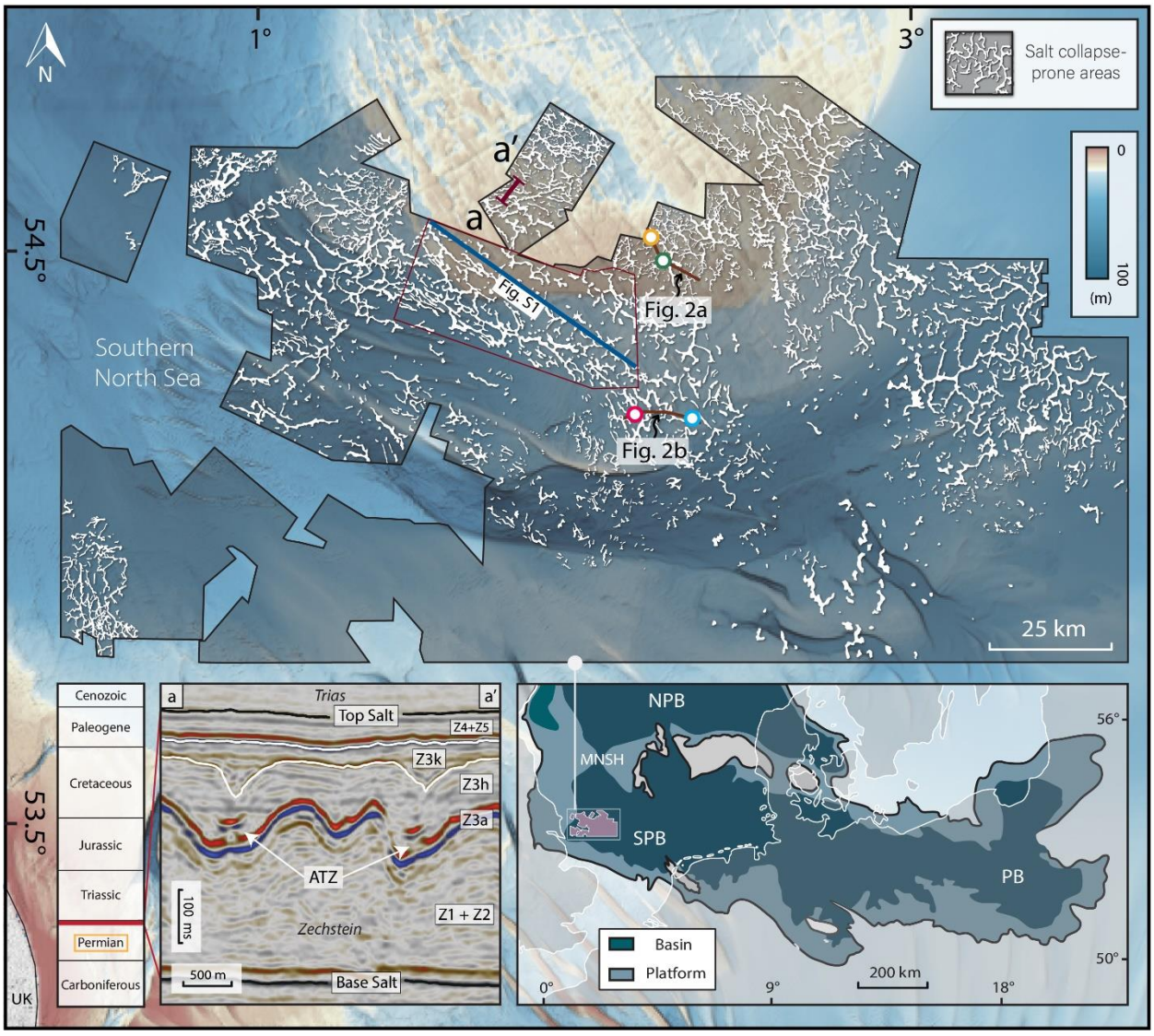

337 **Figure 2**

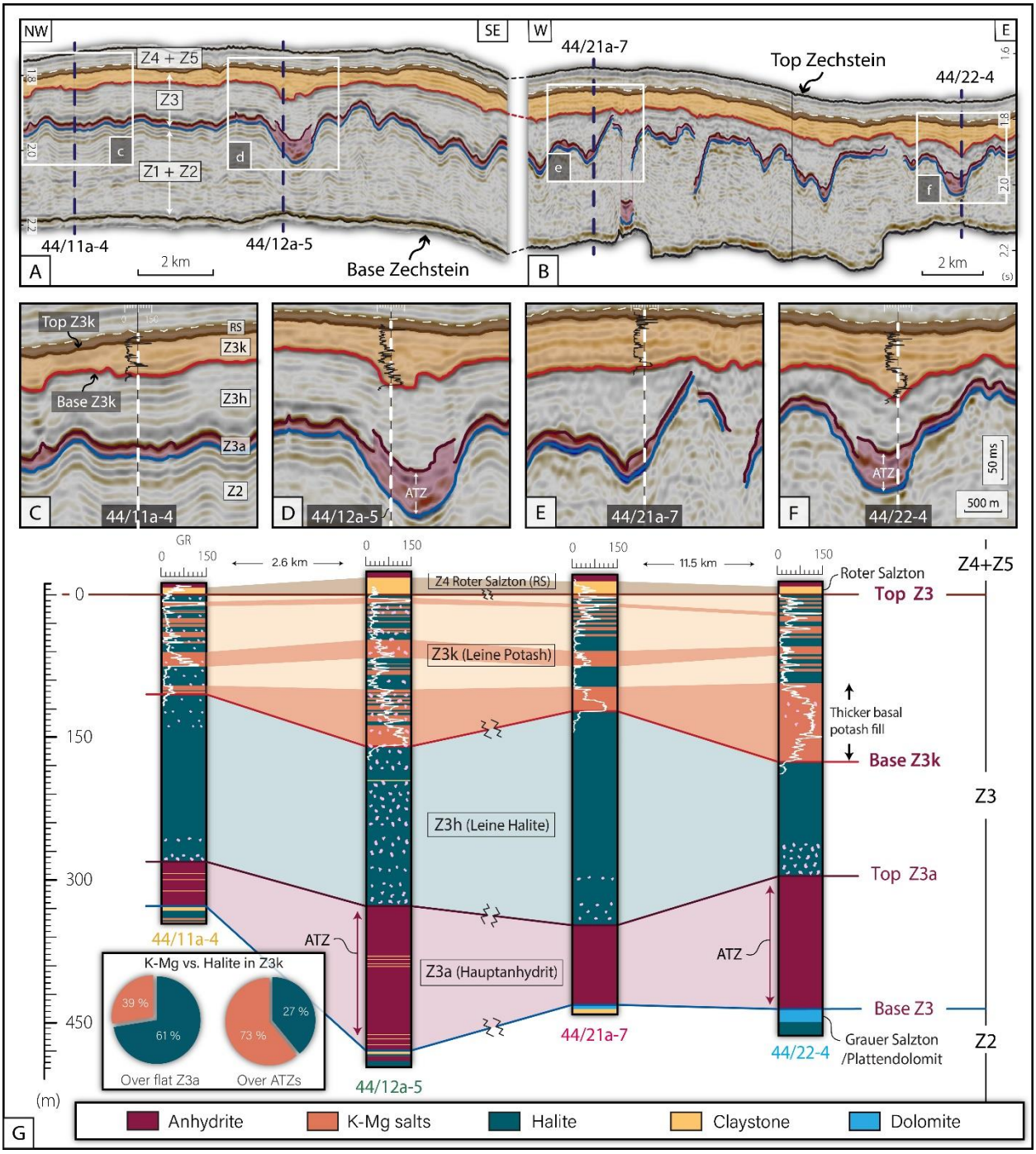

338

339

340

Figure 3

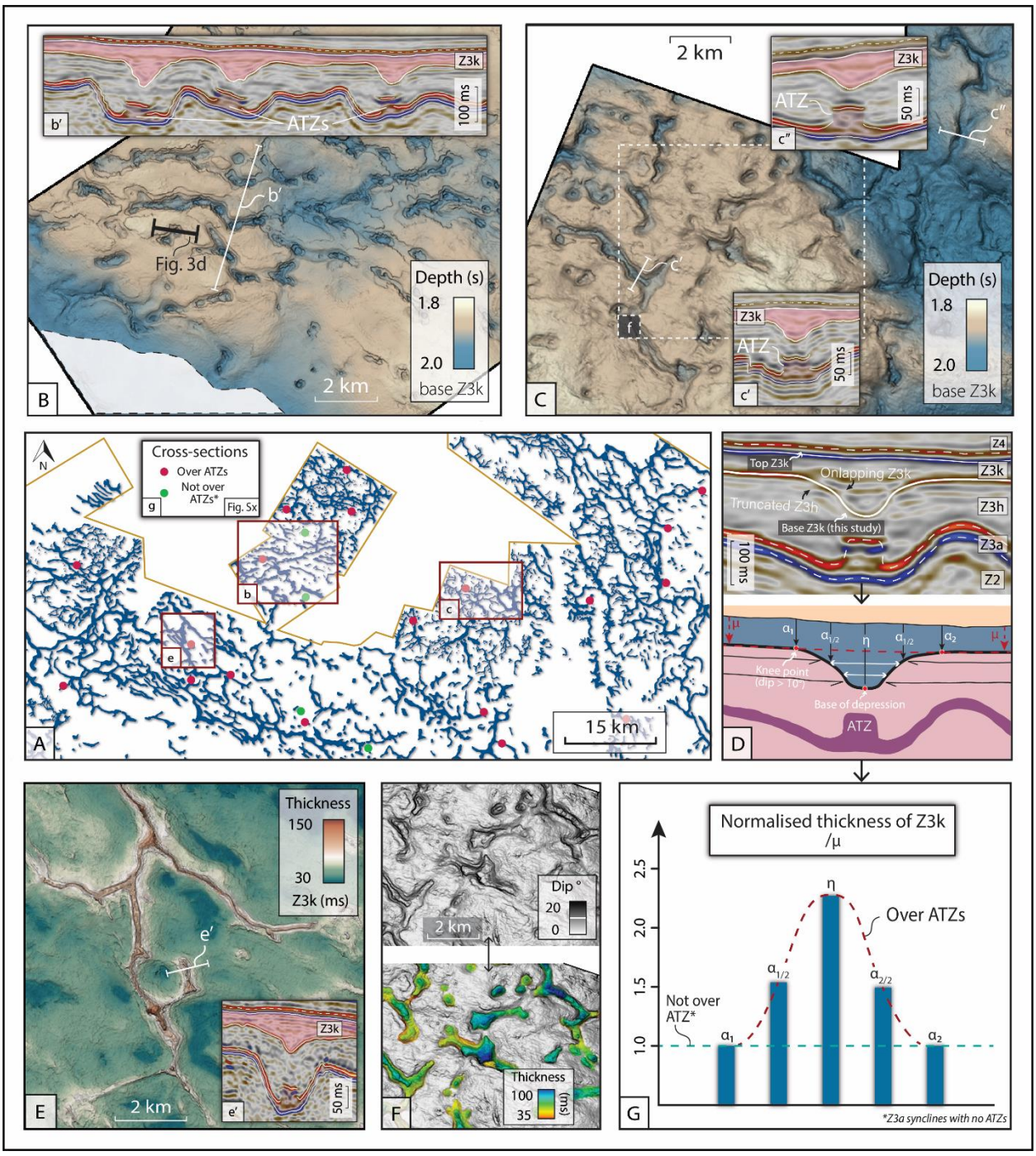
B
b′
ATZs
Z3k
100 ms
Fig. 3d
Depth (s)
1.8
2.0
base Z3k
2 km
C
2 km
ATZ
c″
c′
f
50 ms
A
Cross-sections
Over ATZs
Not over ATZs*
g
Fig. 5x
15 km
D
Z4
Top Z3k
Onlapping Z3k
Z3k
Truncated Z3h
Z3h
Base Z3k (this study)
Z3a
Z2
Knee point
Base of depression
ATZ
E
Thickness
150
30
Z3k (ms)
e′
F
Dip °
20
0
Thickness
100
35
(ms)
G
Normalised thickness of Z3k /μ
Over ATZs
Not over ATZ*
*Z3a synclines with no ATZs

Figure 4

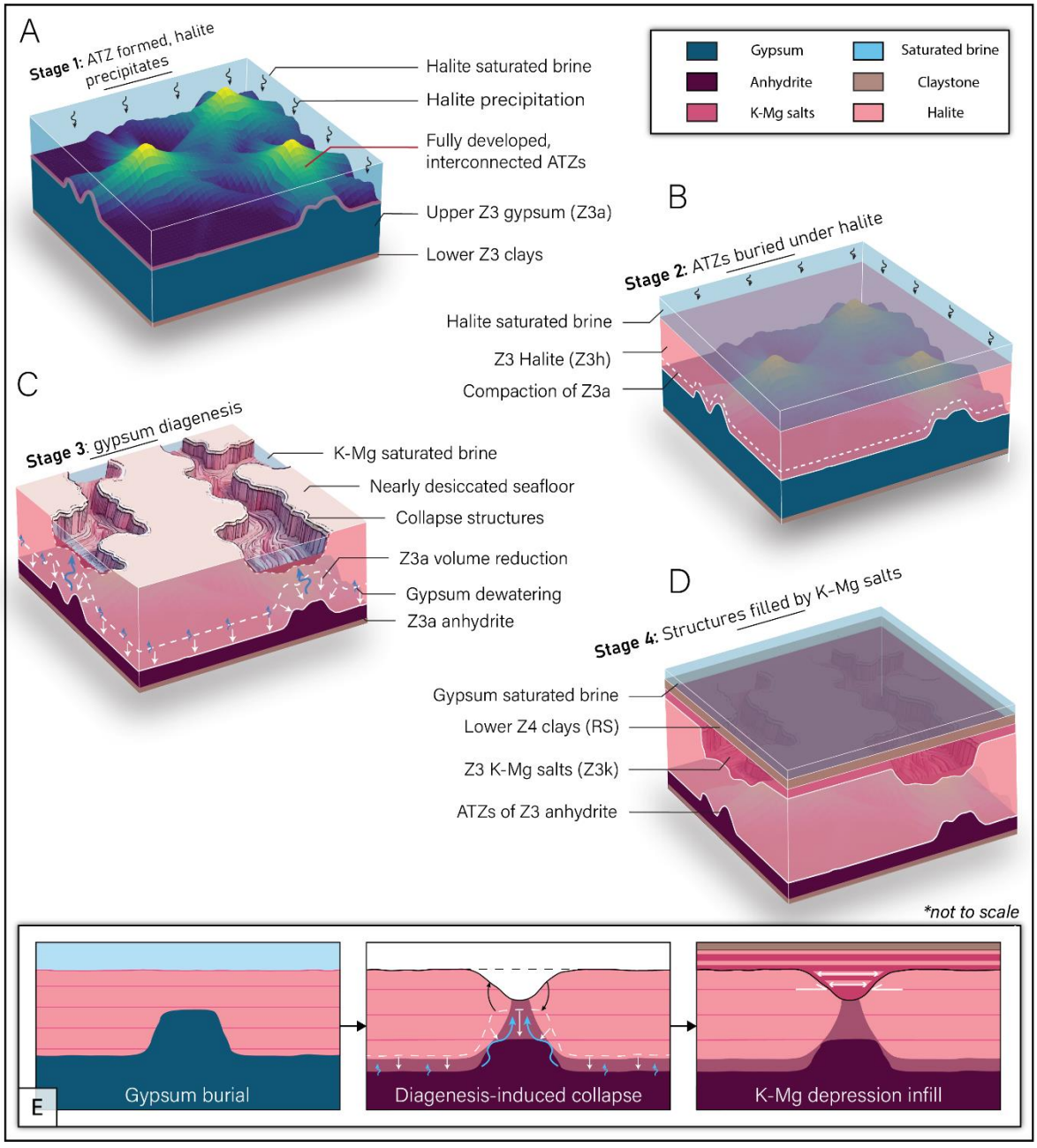
A
Stage 1: ATZ formed, halite precipitates
Halite saturated brine
Halite precipitation
Fully developed, interconnected ATZs
Upper Z3 gypsum (Z3a)
Lower Z3 clays
Gypsum
Anhydrite
K-Mg salts
Saturated brine
Claystone
Halite
B
Stage 2: ATZs buried under halite
Halite saturated brine
Z3 Halite (Z3h)
Compaction of Z3a
C
Stage 3: gypsum diagenesis
K-Mg saturated brine
Nearly desiccated seafloor
Collapse structures
Z3a volume reduction
Gypsum dewatering
Z3a anhydrite
D
Stage 4: Structures filled by K-Mg salts
Gypsum saturated brine
Lower Z4 clays (RS)
Z3 K-Mg salts (Z3k)
ATZs of Z3 anhydrite
*not to scale
E
Gypsum burial
Diagenesis-induced collapse
K-Mg depression infill

Supplemental Material:

Seismic-To-Well Tie And Mapping

We generated synthetic seismograms to tie lithological and seismic-stratigraphic boundaries interpreted from the wells and seismic data, respectively (Fig. S2). Borehole data included drilling cuttings (9m sampling frequency) and petrophysical logs (e.g., GR, DT, RHOB), which together enabled a detailed stratigraphic analysis of Z3k and mapping of its bounding seismic reflections (base and top Z3k). Seismic and well-logs show that: (1) top Z3k corresponds to a positive reflection (Fig. S2), marking the downward transition from Z4 claystone to K-Mg-rich layers, with GR logs showing values up to 150 API; and (2) base Z3k corresponds to another positive reflection (Fig. S2), corresponding to a thick Z3k K-Mg-rich layer directly overlying the halite-dominated Z3h.

Key seismic horizons identified in synthetic seismograms were mapped across the study area (Fig. S6) and interpreted on a seeded auto-tracked horizon picking from an original ~25 x 25m manual grid picking.

Zechstein Stratigraphy

Evaporite accumulation was strongly influenced by environmental variations, which led to the subdivision of the stratal architecture of the whole unit (e.g., Tucker, 1991; Mitchum and van Wagoner; 1991; Goodall et al., 1992). Four to five (Z1-Z5, Figure 2) main Zechstein seismo-stratigraphic cycles have been recognised and correlated across the (Taylor, 1998; Geluk, 2005; Peryt et al., 2010) and correspond to main “evaporitic cycles” (Warren, 2006), leading to a wide variety of basin-scale lithologies: shale, carbonates, sulphates, halite and K–Mg salts anhywhere in the central SPB (Figure 2) (e.g., Geluk et al., 2007: Biehl, 2014; Raith et al., 2016; Pichat, 2022).

Typically, the basal unit in each cycle consists of carbonates, interbedded and then overlain by anhydrite, followed by thick deposits of halite, capped with an interbedded mixture of halite, anhydrite, and K-Mg (potash) salts (Smith, 1981; Ziegler, 1990; Taylor, 1998; Peryt et al., 2010). In the Zechstein Group, the ratio of carbonates to evaporites declines progressively from the older cycles to the more recent ones (Taylor, 1998; Geluk, 1999) (Figure 2).

Stratigraphy Of The Z3k

The Z3 cycle follows a complete evaporitic sequence (Warren, 2006) beginning with clastic deposits, transitioning with carbonate and sulphate layers, and progressing to halite before culminating in K-Mg salts (Smith and Crosby, 1979). In this study, the upper elements of the Z3 (Z3k) unit were primarily examined as they are central to this analysis. The Z3k (Fig. 2c-g), documented mainly (1) from mining sites overlying salt structures in the southeast UK (Armstrong et al., 1951; Stewart, 1963; Smith, 1979, 1981; Talbot et al., 1982; Kemp et al., 2016), Germany (Richter-Bernburg, 1955; Herrmann and Knipping, 1993; Krupp, 2005) Poland (Podemski 1974, Dawidowski 1976, Czapowski 2006, Czapowski and bukowski 2010; Czapowski 2012) and (2) from offshore data (e.g., petrophysical logs and drill cuttings, Smith and Crosby, 1979; Pichat, 2022), is a chloride-dominated layer over the Z3 halite, and comprise mainly sylvinite, carnallite and halite with minor occurrences of anhydrite, kieserite, and bischofite (Herrmann, 1991, Kemp et al., 2016; Raith et al., 2017). The Z3k is 10m thick in marginal areas, with increasing thickness distally reaching up to 40, and even more (90 m) due to alleged halokinetic deformation (Smith and Crosby, 1979; Czapowski and bukowski 2010; Raith et al., 2017). Its formation involved primary evaporitic deposition and early diagenetic recrystallisation reflecting salinity fluctuations and basin dynamics (Krupp, 2005; Czapowski et al., 2012; Raith et al., 2017). The sporadic

394 presence of bischofite “lakes”, /isolated depocenters in Poland (Hanczke, 1969; Krupp, 2005;
395 Czapowski et al., 2012) and the Netherlands (Pichat, 2022), combined with the occurrence of
396 "desiccation cracks" within the Z3k (Tomassi-Morawiec et al., 2008, 2009; Czapowski and
397 Bukowski, 2010; Czapowski et al., 2012; Raith et al., 2017), suggests episodic exposure and drying
398 of the basin floor, under isolated conditions. Overlying the Z3k is the basal Z4 *Roter Salzton*, or
399 “red salt clay” (Fig. 2; Richter-Bernburg, 1955, van Gent, 2011; Barabasch, 2019, Grant et al.,
400 2019), a decametric, almost perfectly isopachous basinwide clay layer capping the Z3 potash
401 traceable all over the SPB from the UK to the SE Netherlands.
402

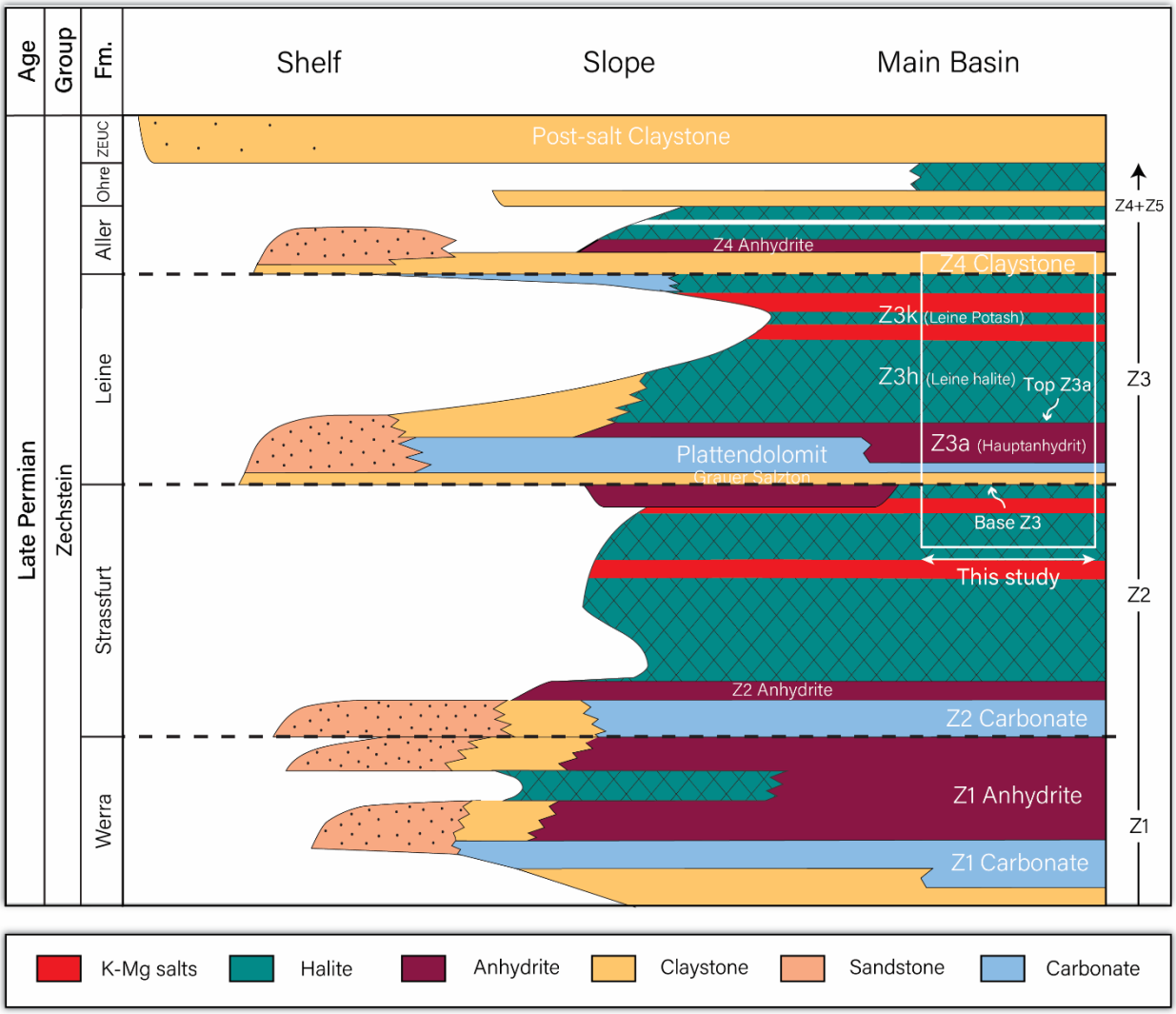

403

404 **Fig. S1** Simplified lithostratigraphic chart of the Zechstein Group in the SNS. The white rectangle represents the seismo-
405 stratigraphy of interest (see cross section aa' of Figure 1 for corresponding seismic facies). Chart modified after Geluk (1999),
406 Geluk et al. (2007), Strozyk et al. (2014), Barabasch et al. (2019), and Pichat (2022).

407

408

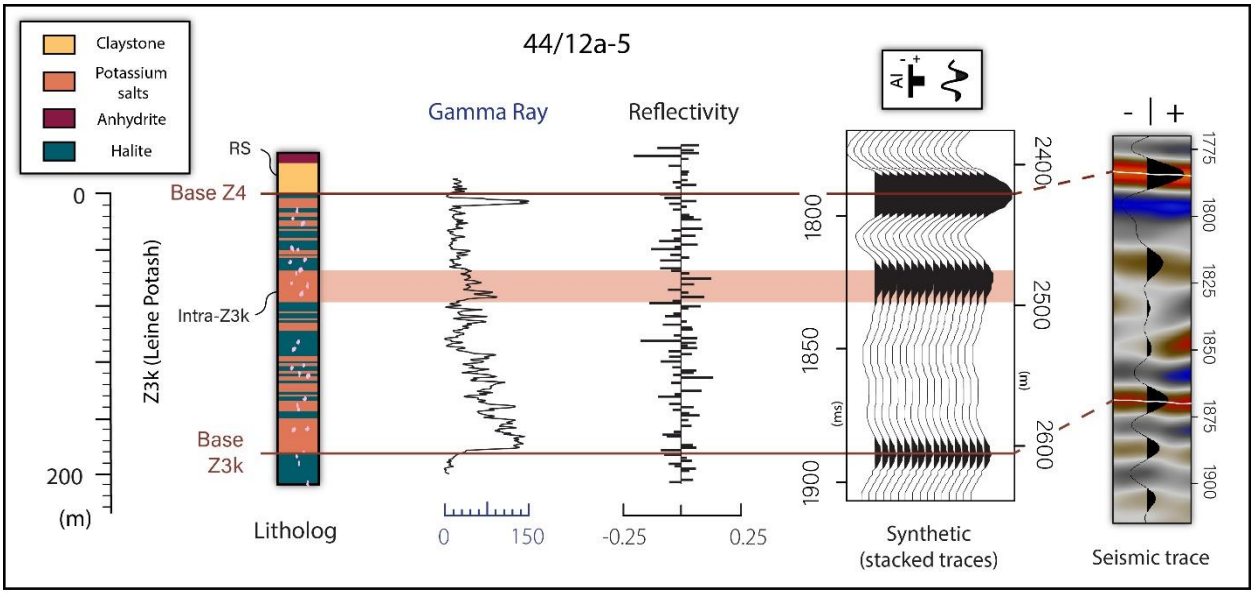

409

410 **Fig. S2** Modelled synthetic seismogram, lithostratigraphy and seismic to well-tie approach for borehole 44/12a-5 (location in
411 Figures 1 and S2). From left to right: Litholog—interpreted lithology log from drilling cuttings obtained from the mudlogging
412 unit (vertical resolution of 9 m) and petrophysical logs. Z3a petrophysical logs: GR—Gamma Ray scaled in API units. Seismic
413 trace over seismic data from the SNS MegaSurvey dataset. The synthetic seismogram is shown with primaries and multiples, and
414 generated with a 1ms sample interval, the convolution of the reflectivity series is applied with a bandpass filter having a low cut
415 of 5 Hz and a high cut of 50 Hz. The seismic wiggle measured depth (MD, two-way time, in ms) is referenced to seismic datum
416 of mean sea level. Pink dots within litholog represent anhydrite inclusions.

417

418

419

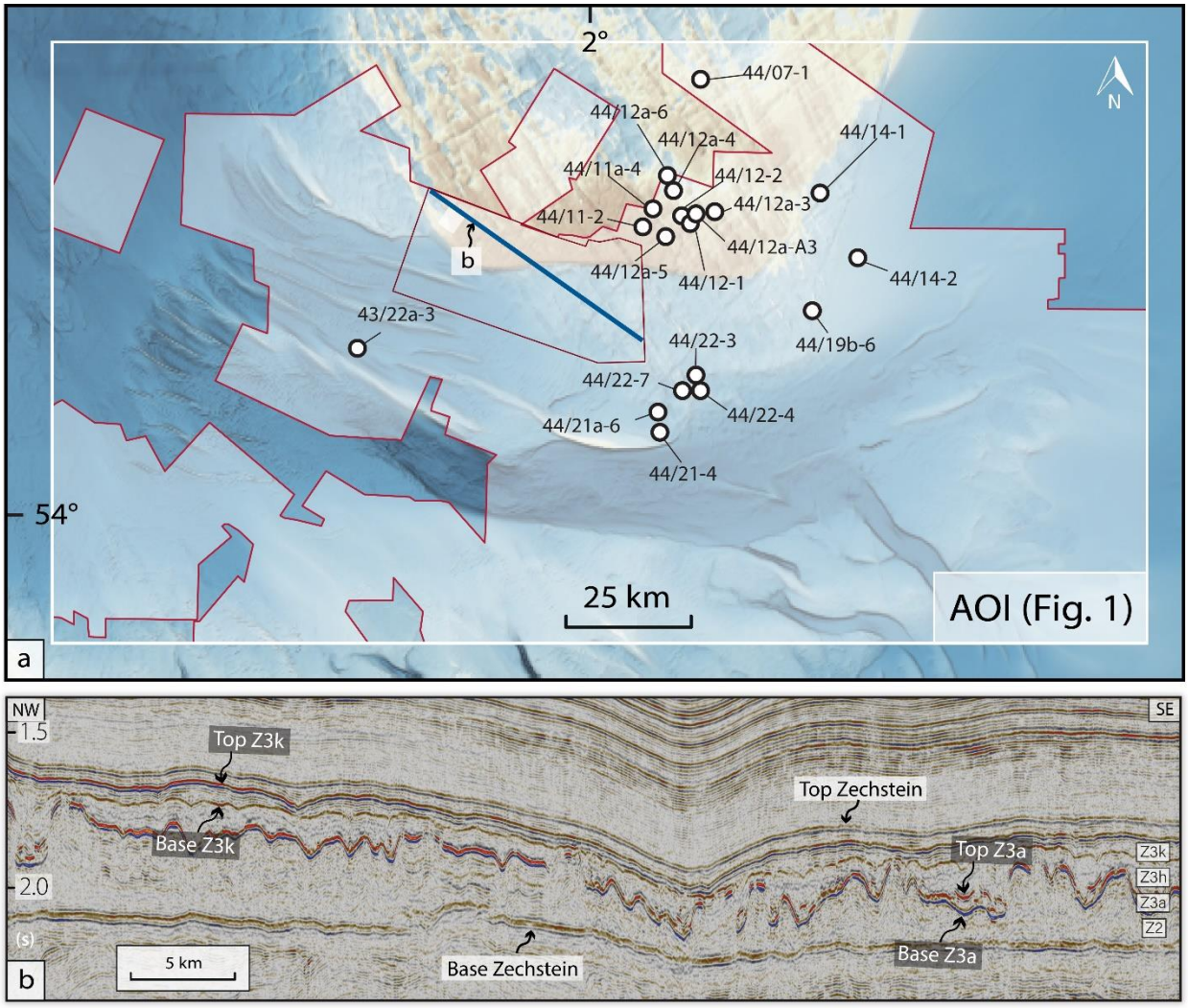

420

421 **Fig. S3 a**. Location of the 19 wells studied. **b**. Additional uninterpreted regional seismic reflection profile (from the Cavendish

422 dataset, location in a.) showing how halokinetics affects the Zechstein salt. The Z3a unit appears strongly folded; and shows how

423 the Z3k thickens due to Cenozoic deformation and salt remobilisation (e.g., Brennan et al., 2023).

424

425

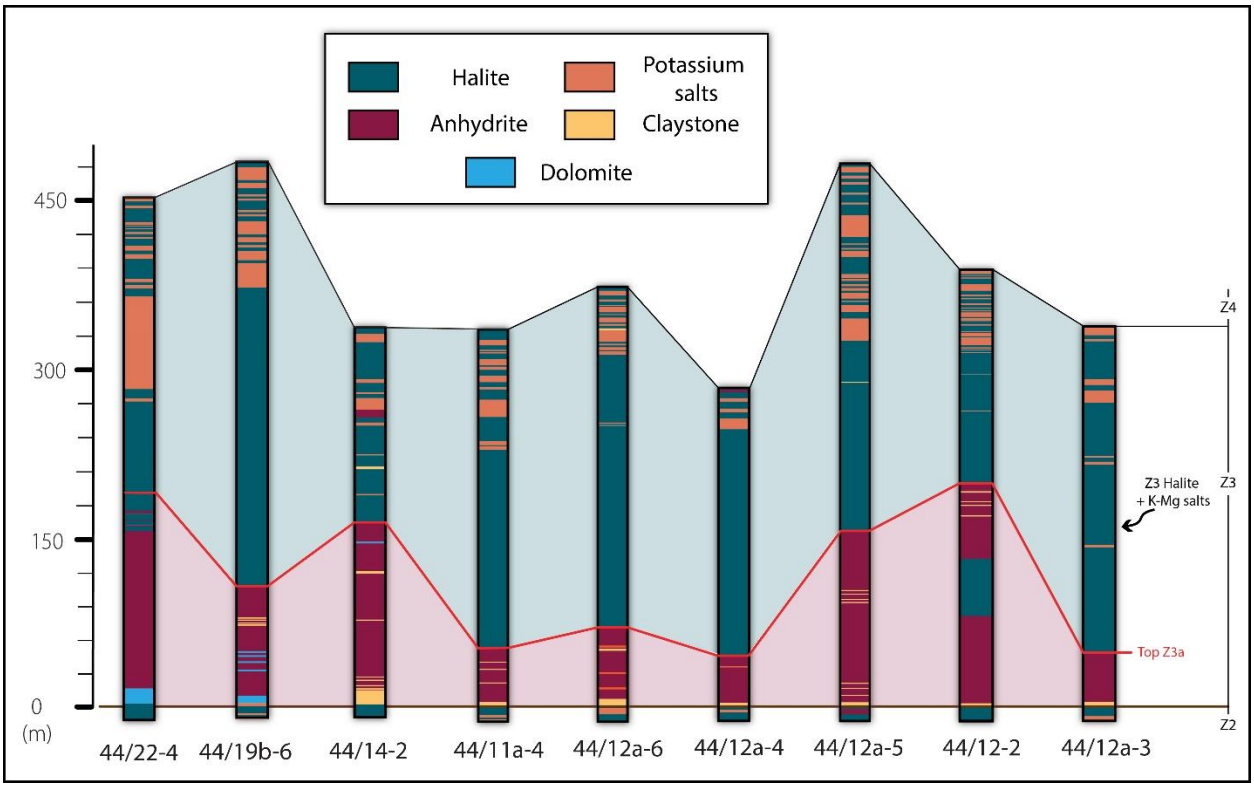

Fig. S4 Borehole additional information showing the Z3a lithology. Stratigraphic correlation (datum for correlation is defined as base Z3), derived from cuttings and petrophysical logs (obtained from https://ndr.nstauthority.co.uk/), borehole location in Figure S2.

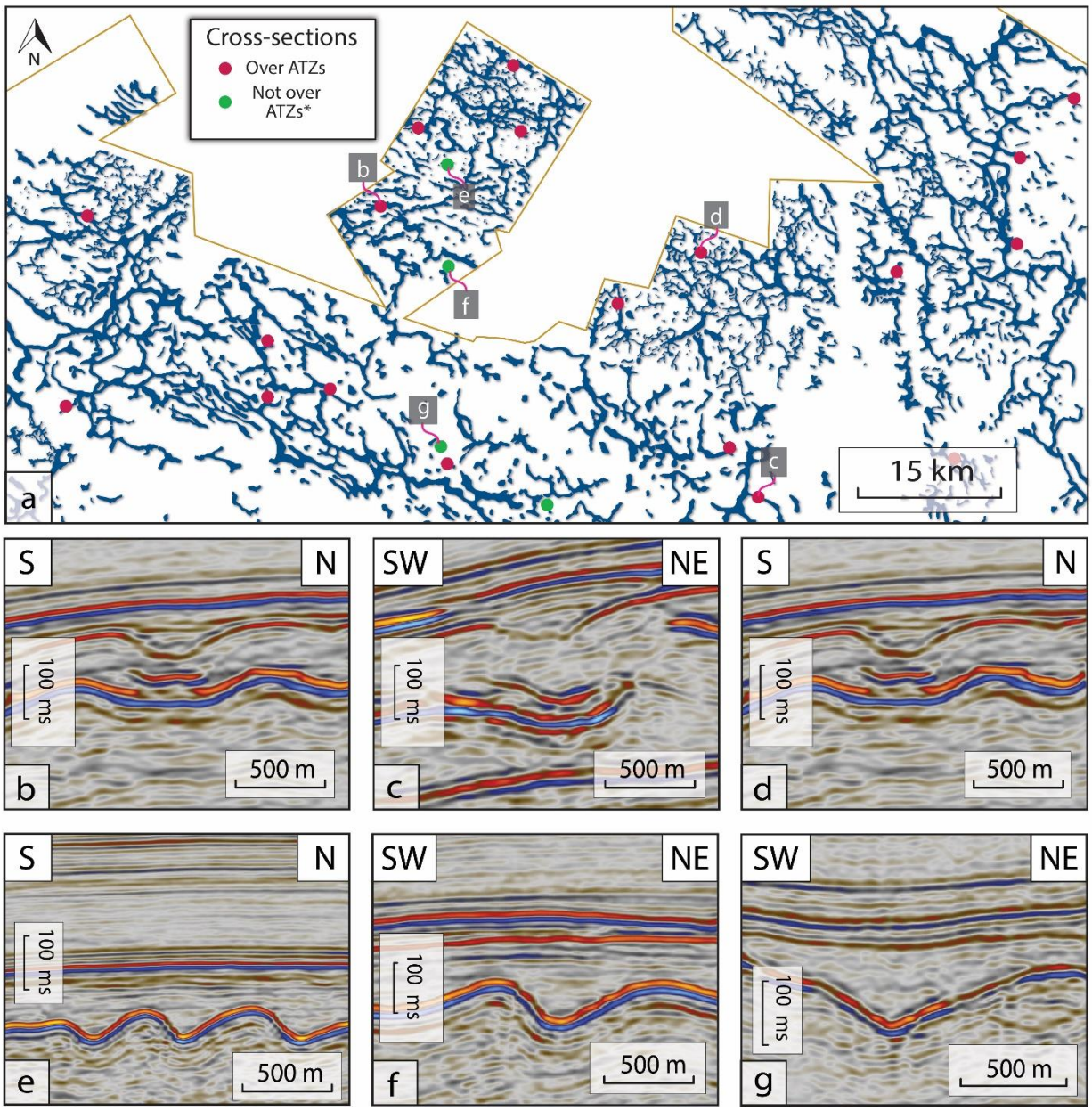

Fig. S5. Map and seismic cross-sections showing the relationship between ATZs and Z3k depressions. **b–d**. Cross-sections illustrating depressions consistently forming above ATZs. **e–g.** Cross-section showing no depressions where the Z3a lacks ATZs, even when folded.

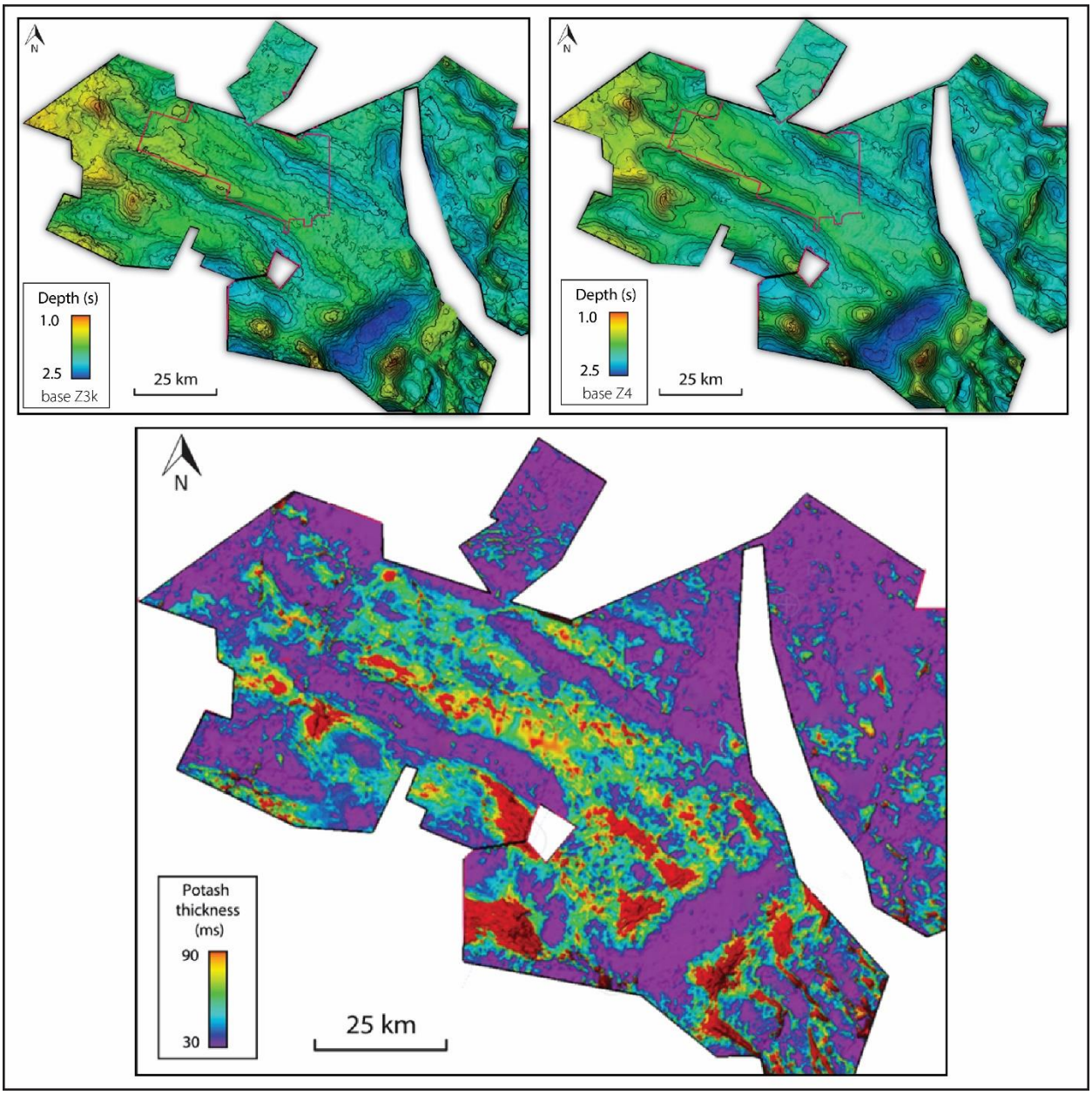

437

438 **Fig. S6** Structural and thickness maps for the study area located in Fig. 1.

439

a

Well Number	Hauptanhydrit (ft)	Hauptanhydrit (m)	Thickness KMg (ft)	Thickness Kmg (m)	Z3k Halite (m)	Z3k total (ft)	Z3k (m)	% of Kmg Salts within Z3k
Not over ATZs								
43_22a-3	183	55.7784	100	30.48	42.672	240	73.152	41.66666667
44_07-1	180	54.864	50	15.24	64.008	260	79.248	19.23076923
44_11-2	144	43.8912	110	33.528	42.672	250	76.2	44
44_11a-4	159	48.4632	130	39.624	39.624	260	79.248	50
44_12-1	157	47.8536	40	12.192	36.576	160	48.768	25
44_12a-3	145	44.196	80	24.384	47.244	235	71.628	34.04255319
44_12a-4	143	43.5864	40	12.192	33.528	150	45.72	26.66666667
44_12a-6	202	61.5696	110	33.528	27.432	200	60.96	55
44_12a-A3	191	58.2168	155	47.244	38.1	280	85.344	55.35714286
44_14-1	138	42.0624	70	21.336	42.672	210	64.008	33.33333333
44_21-4	126.3	38.49624	110	33.528	48.768	270	82.296	40.74074074
44_21a-6	118	35.9664	150	45.72	60.96	350	106.68	42.85714286
44_22-3	143	43.5864	120	36.576	54.864	300	91.44	40
Average		47.57928	97.30769231	29.65938462	44.54769231	243.4615385	74.207077	39.06884735
Over ATZs								
44_12-2	528	160.9344	170	51.816	33.528	280	85.344	60.71428571
44_12a-5	505	153.924	350	106.68	51.816	520	158.496	67.30769231
44_14-2	481	146.6088	210	64.008	9.144	240	73.152	87.5
44/19b-6	310	94.488	190	57.912	30.48	290	88.392	65.51724138
44_22-4	470	143.256	410	124.968	39.624	540	164.592	75.92592593
44_22-7	283	86.2584	280	85.344	24.384	360	109.728	77.77777778
Average:		130.9116	268.3333333	81.788	31.496	371.6666667	113.284	72.45715385

b

	Over ATZs																									No over ATZs					
Cross section	CS1	CS2	CS3	CS4	CS5	CS6	CS7	CS8	CS9	CS10	CS11	CS12	CS13	CS14	CS15	CS16	CS17	CS18	CS19	CS20	CS21	CS22	CS23	CS24	CS25	CS26	CS27	CS29	CS30	CS31	CS32	CS33
α1	1	1	1	1	1	1	1	1	1	1	1	1	1	1	1	1	1	1	1	1	1	1	1	1	1	1	1	1	1	1	1	1
α1/2	1.3	1.25	1.77	1.2	1.35	1.4	1.46	1.4	1.5	1.22	1.7	1.3	1.2	1.8	2.2	1.3	2.2	1.75	2.57	1.5	1.3	1.5	1.25	1.4	1.54	1.7	1.36	1	1	1	1	1
η	3.6	1.93	2.62	1.7	1.85	2.3	2.23	1.9	2.5	1.52	2	2	1.7	2.9	2.5	2	2.9	2.375	4.86	2.3	1.6	1.95	1.67	2	2.08	2.4	1.91	1	1	1	1	1
α2/2	1.3	1.29	1.69	1.2	1.25	1.6	1.31	1.4	1.5	1	1.4	1.2	1.2	1.8	1.5	1.1	1.7	1.625	2.71	1.6	1.4	1.55	1.33	1.5	1.69	1.8	1.55	1	1	1	1	1
α2	1	1	1	1	1	1	1	1	1	1	1	1	1	1	1	1	1	1	1	1	1	1	1	1	1	1	1	1	1	1	1	1

Fig. S7 Summary of metrics used in this study. **A**. Tabulated data comparing the thicknesses of Hauptanhydrit (Z3a), K-Mg salts, and halite (Z3h) within and outside ATZs. Averaged thicknesses and proportions of K-Mg salts within the Z3k unit are also provided, highlighting significant differences between areas overlying ATZs and those that do not. **B**. Cross-section indices categorising sections over and outside ATZs, indicating the distribution and structural variability across study regions.

SUPPLEMENTARY REFERENCES CITED

Armstrong, G., Dunham, K. C., Harvey, C. O., Sabine, P. A., & Waters, W. F. (1951). The paragenesis of sylvine, carnallite, polyhalite, and kieserite in eskdale borings nos. 3, 4, and 6, north-east yorkshire. Mineralogical magazine and journal of the Mineralogical Society, 29(214), 667-689.

Barabasch, J., Urai, J.L., Raith, A.F., and De Jager, J., 2019. The early life of a salt giant: 3D

seismic study on syntectonic Zechstein salt and stringer deposition on the Friesland Platform, Netherlands. Z. Dtsch. Ges. Für Geowiss., 170, 273–288. https://doi.org/10.1127/zdgg/2019/0186.

Biehl, B.C., Reuning, L., Strozyk, F., and Kukla, P.A., 2014. Origin and deformation of intra-salt sulphate layers: an example from the Dutch Zechstein (Late Permian). International Journal of Earth Sciences, 103, 697–712. https://doi.org/10.1007/s00531-014-0999-4.

Bornemann, O., 1991. Zur Geologie des Salzstocks Gorleben nach den Bohrergebnissen. - BfS-Schriften, 4: 1-67; Salzgitter.

Brennan, C., Preiss, A., and Adam, J., 2023. Three-dimensional seismic classification of salt structure morphologies across the Southern North Sea. AAPG Bulletin, 107(12), 2141–2167.

Czapowski G., 2006. Permskie sole potasowo-magnezowe na obszarze centralnej i poludniowo-zachodniej Polski – obecny stan rozpoznania. Przeglad Geologiczny, 54, 4, 317.

Czapowski, G., and Bukowski, G., 2010. Halokinetic impact on Zechstein salt deposition. Geological Quarterly, 54, 20–36.

Czapowski, G., Tomassi-Morawiec, H., Toboła, T., & Tadych, T. (2012). Geology, geochemistry and petrological characteristics of potash salt units from PZ2 and PZ3 Zechstein (Late Permian) cycles in Poland. *Geol. Geophys. Environ*, *38*(2), 153-188.

Dawidowski S., 1976. Obecne rozpoznanie koncentracji soli potasowych mlodszych (K3) w okolicy Nowej Soli i perspektywy ich gospodarczego zastosowania. *Przeglad Geologiczny*, 24, 9, 545–546.

Hanczke T., 1969. Mineralogia i petrogra□ a soli cechsztynskich kopalni Klodawa. *Prace*

Muzeum Ziemi, 16, 3–52.

Herrmann, A. G., & Borstel, L. (1991). The composition and origin of fluid inclusions in Zechstein evaporites of Germany. *Neues Jahrbuch für Mineralogie Monatshefte*, (6), 263-269.

Geluk, M., 1999. Late Permian (Zechstein) rifting in the Netherlands; models and implications for petroleum geology. Pet. Geosci. 5, 189–199. https://doi.org/10.1144/petgeo.5.2.189.

Geluk, M.C., 2005. Stratigraphy and Tectonics of Permo-Triassic Basins in the Netherlands and Surrounding Areas. PhD thesis, Utrecht University, Utrecht, The Netherlands.

Geluk, M.C., Wong, T.E., Batjes, D.A.J., and De Jager, J., 2007. Permian. Geology of the Netherlands, 63–83.

Goodall, I.G.; Harwood, G.M.; Kendall, A.C.; McKie, T.; Tucker, M.E., 1992. Discussion on sequence stratigraphy of carbonate-evaporite basins: Models and application to the Upper Permian (Zechstein) of northeast England and adjoining North Sea. J. Geol. Soc. 149, 1050–1054.

Grant, R.J., Underhill, J.R., Hernández-Casado, J., Barker, S.M., and Jamieson, R.J., 2019. Upper Permian Zechstein Supergroup carbonate-evaporite platform palaeomorphology in the UK southern North Sea. Marine and Petroleum Geology, 100, 484–518.

Herrmann, A. G., & Knipping, B., 1993. Waste disposal and evaporites: contributions to long-term safety (Vol. 45). Springer-Verlag.

Kemp, S. J., Smith, F. W., Wagner, D., Mounteney, I., Bell, C. P., Milne, C. J., ... & Pottas, T. L. (2016). An improved approach to characterize potash-bearing evaporite deposits, evidenced in North Yorkshire, United Kingdom. Economic Geology, 111(3), 719-742.

Krupp, R. E., 2005. Formation and chemical evolution of magnesium chloride brines by

498 evaporite dissolution processes—Implications for evaporite geochemistry. Geochimica et
499 Cosmochimica Acta, 69(17), 4283-4299.
500 Mitchum Jr, R.M. and van Wagoner, J.C., 1991. High-frequency sequences and their stacking
501 patterns: sequence-stratigraphic evidence of high-frequency eustatic cycles. Sedimentary
502 geology, 70(2-4), pp.131-160.
503 Peryt, T.M., Halas, S., and Petrivna Hryniv, S., 2010. Sulphur and oxygen isotope signatures of
504 late Permian Zechstein anhydrites, West Poland: seawater evolution and diagenetic
505 constraints. Geological Quarterly, 54(4), 387–400.
506 Pichat, A., 2022. Stratigraphy, paleogeography, and depositional setting of the K–Mg salts in the
507 Zechstein Group of the Netherlands—Implications for the development of salt caverns.
508 Minerals, 12(4), 486.
509 Podemski M., 1974. Stratygrafia a utworów cechsztynskich zachodniej czesci niecki pónocno-
510 sudeckiej. Kwartalnik Geologiczny, 18, 4, 729–748.
511 Raith, A.F., Strozyk, F., Visser, J., and Urai, J.L., 2016. Evolution of rheologically
512 heterogeneous salt structures: a case study from the NE Netherlands. Solid Earth, 7(1),
513 67–82. https://doi.org/10.5194/se-7-67-2016.
514 Raith, A.F., Strozyk, F., Visser, J., & Urai, J.L., 2017. Evolution of rheologically heterogeneous
515 salt structures: a case study from the NE Netherlands. Solid Earth, 7, 67–82.
516 Richter-Bernburg, G., 1955. Stratigraphische Gliederung des deutschen Zechsteins. Z. dt. geol.
517 Ges. 105, 843–854.
518 Smith, D.B., and Crosby, A., 1979. The regional and stratigraphical context of Zechstein 3 and 4
519 potash deposits in the British sector of the southern North Sea and adjoining land areas.
520 Economic Geology, 74, 397–408.

Smith, D.B., 1979. Rapid marine transgressions and regressions of the upper Permian Zechstein Sea. J. Geol. Soc. 136, 155–156. https://doi.org/10.1144/gsjgs.136.2.0155.

Smith, D.B., 1981. The evolution of the English Zechstein basin.

Stewart, F. H., 1963. *Marine evaporites*. US Government Printing Office.

Strozyk, F., Urai, J.L., van Gent, H., De Keijzer, M., Kukla, P.A., 2014. Regional variations in the structure of the Permian Zechstein 3 intrasalt stringer in the northern Netherlands: 3D seismic interpretation and implications for salt tectonic evolution. Interpretation 2, SM101–SM117. https://doi.org/10.1190/INT-2014-0037.1.

Talbot, C. J., Tully, C. P., & Woods, P. J. E. (1982). The structural geology of Boulby (potash) mine, Cleveland, United Kingdom. Tectonophysics, 85(3-4), 167-204.

Taylor, J.C.M., 1998. Upper Permian—Zechstein, in: Petroleum Geology of the North Sea. John Wiley & Sons, Ltd, pp. 174–211. https://doi.org/10.1002/9781444313413.ch6.

Tomassi-Morawiec H., Czapowski G. & Sztyrak T., 2008b. Opróbowanie geochemiczne rdzeni z utworów solnych cechsztynu w otworach wiertniczych G-34, G-39 i G-16 zlokalizowanych w KS i PMTiP „Góra". Archiwum IKS Solino SA, Inowroclaw.

Tomassi-Morawiec H., Czapowski G., Bornemann O., Schramm M. & Misiek G., 2009. Wzorcowe profile bromowe dla solnych utworów cechsztynu w Polsce. *Gospodarka Surowcami Mineralnymi*, 25, 2, 75–143.

Tucker, M.E., 1991. Sequence stratigraphy of carbonate-evaporite basins: models and application to the Upper Permian (Zechstein) of northeast England and adjoining North Sea. J. Geol. Soc. 148, 1019–1036. https://doi.org/10.1144/gsjgs.148.6.1019.

Warren, J.K., 2006. Evaporites: Sediments, Resources and Hydrocarbons. Springer, Berlin, Heidelberg. https://doi.org/10.1007/3-540-32344-9.

Ziegler, P.A., 1990. Geological atlas of western and central Europe (Vol. 52). The Hague: Shell Internationale Petroleum Maatschappij BV.